

Spin dynamics simulations of excitations and critical dynamics in RbMnF_3

D. P. LANDAU, Shan-Ho TSAI and Alex BUNKER *

*Center for Simulational Physics
The University of Georgia
Athens, GA 30602*

(Received November 19, 2013)

Spin-dynamics simulations have been used to investigate the dynamic behavior of RbMnF_3 , treating it as a classical Heisenberg antiferromagnet on a simple cubic lattice. Time-evolutions of spin configurations were determined numerically from coupled equations of motion for individual spins using a new algorithm which is based on Suzuki-Trotter decompositions of exponential operators. The dynamic structure factor was calculated from the space- and time-displaced spin-spin correlation function. The crossover from hydrodynamic to critical behavior of the dispersion curve and spin-wave half-width was studied as the temperature was increased towards the critical value. The dynamic critical exponent was estimated to be $z = (1.43 \pm 0.03)$, which is slightly lower than the dynamic scaling prediction, but in good agreement with a recent experimental value. Comparisons are made of both the dispersion curve and the lineshapes obtained from our simulations with very recent experimental results for RbMnF_3 are presented.

KEYWORDS: spin dynamics, critical dynamics

§1. Introduction

RbMnF_3 has been the subject of numerous experimental and theoretical investigations since it is a good physical realization of an isotropic three-dimensional Heisenberg antiferromagnet. Early experimental studies^{1,2,3,4} showed that the Mn^{2+} ions, with spin $S = 5/2$, form a simple cubic lattice structure with a nearest-neighbor exchange constant $J^{exp} = (0.58 \pm 0.06)$ meV and a second-neighbor interaction constant of less than 0.04 meV [both defined using the exchange constant to be shown in Eq. (3.4), the normalization used here differs from that of Ref.4 by a factor of two]. Magnetic ordering with antiferromagnetic alignment of spins occurs below the critical temperature $T_c = 83\text{K}$. The magnetic anisotropy is very low, about 6×10^{-6} of the exchange field, and no deviation from cubic symmetry was seen at T_c .^{5,6}

Both the static properties and the dynamic response of RbMnF_3 have been examined through neutron scattering experiments. Windsor and co-workers⁴ looked at spin-waves at low temperatures and mapped out the dispersion curve. The early work of Tucciarone *et al*⁷ found that in the critical region the neutron scattering function has a central peak (peak at zero frequency transfer) and a spin-wave peak. Later experiments by Cox *et al*⁸ observed a small central peak below T_c as well. The more recent study by Coldea *et al*⁹ also found central peaks for $T \leq T_c$, in agreement with previous work. From the theoretical side, renormalization-group (RNG) below T_c ¹⁰ predicts spin-wave peaks, and a central peak in the longitudinal component of the neutron scattering func-

tion; however, at T_c both renormalization-group¹¹ and mode-coupling¹² theories predict only the presence of a spin-wave peak. The experimentally observed central peak is thought to be caused by spin diffusion resulting from nonlinearities in the dynamical equations.⁷ Coldea *et al*⁹ also obtained the most precise experimental estimate of the dynamic critical exponent, $z = (1.43 \pm 0.04)$. This is slightly smaller than the predicted value¹³ of $z = 1.5$ for an isotropic Heisenberg antiferromagnet in $d = 3$ dimensions.

Extensive Monte Carlo studies measured the static properties of classical Heisenberg magnets but could not examine the true dynamics of the systems. Several large-scale spin-dynamics simulations have probed the behavior of various classical systems;^{14,15} however, there are no direct comparisons to experimental data for physical systems. In the present work we report large-scale simulations of the dynamic behavior of the Heisenberg antiferromagnet on a simple cubic lattice, and make direct comparison with experimental data.

§2. Model and Methods

The classical Heisenberg antiferromagnet is defined by the Hamiltonian

$$\mathcal{H} = J \sum_{\langle \mathbf{r}\mathbf{r}' \rangle} \mathbf{S}_{\mathbf{r}} \cdot \mathbf{S}_{\mathbf{r}'}, \quad (2.1)$$

where $\mathbf{S}_{\mathbf{r}} = (S_{\mathbf{r}}^x, S_{\mathbf{r}}^y, S_{\mathbf{r}}^z)$ is a three-dimensional classical spin of unit length at site \mathbf{r} and $J > 0$ is the antiferromagnetic coupling constant between nearest-neighbor pairs of spins. All simulations were performed using $L \times L \times L$ simple cubic lattices with periodic boundary conditions. The dynamics of the spins are governed

* Present address: Max Planck Institute for Polymer Research, Ackermann Weg 10, Mainz, Germany D-55021-3148

by the coupled equations of motion¹⁶⁾

$$\frac{d}{dt}\mathbf{S}_{\mathbf{r}} = -\mathbf{S}_{\mathbf{r}} \times J \sum_{\langle \mathbf{r}\mathbf{r}' \rangle} \mathbf{S}_{\mathbf{r}'}, \quad (2.2)$$

and the time dependence of each spin can be determined from the integration of these equations.

The dynamic structure factor $S(\mathbf{q}, \omega)$ for momentum transfer \mathbf{q} and frequency transfer ω can be measured by inelastic neutron scattering experiments and is given by

$$S^k(\mathbf{q}, \omega) = \sum_{\mathbf{R}} e^{i\mathbf{q}\cdot\mathbf{R}} \int_{-\infty}^{+\infty} e^{i\omega t} C^k(\mathbf{R}, t) \frac{dt}{\sqrt{2\pi}}, \quad (2.3)$$

where $\mathbf{R} = \mathbf{r} - \mathbf{r}'$, $C^k(\mathbf{R}, t)$ is the space-displaced, time-displaced correlation function, with $k = x, y$, or z , and

$$C^k(\mathbf{R}, t) = \langle S_{\mathbf{r}}^k(t) S_{\mathbf{r}'}^k(0) \rangle - \langle S_{\mathbf{r}}^k(t) \rangle \langle S_{\mathbf{r}'}^k(0) \rangle. \quad (2.4)$$

In the case of antiferromagnets, the wave-vectors are measured with respect to the (π, π, π) point which corresponds to the Brillouin zone center. Note that in the $[1,1,1]$ and $[1,0,0]$ directions the respective first Brillouin zone boundary wave-vectors are $(\pm\pi/2, \pm\pi/2, \pm\pi/2)$ and $(\pm\pi, 0, 0)$.

Using Monte Carlo and spin-dynamics methods,^{14, 15, 16)} we simulated the simple-cubic classical Heisenberg antiferromagnet with $12 \leq L \leq 60$ at the critical temperature¹⁷⁾ $T_c = 1.442929(77)J$ as well as below T_c . (We use units in which Boltzmann's constant $k_B = 1$.) Equilibrium configurations were generated using a hybrid Monte Carlo method^{14, 15)} and the coupled equations of motion were then integrated numerically, using these states as initial spin configurations. Numerical integrations were performed to a maximum time $t_{max} \leq 1000J^{-1}$, using a time step of Δt . The space-displaced, time-displaced correlation function $C^k(\mathbf{R}, t)$ was computed for time-displacements ranging from 0 to t_{cutoff} and extracted from an average over 40 to 80 different time starting points, evenly spaced by $10\Delta t$. As many as 7000 initial configurations were used, although for large lattices this was reduced to as few as 400. For $L = 24$ at $T = 0.9T_c$ the integration was carried out with a time step $\Delta t = 0.01J^{-1}$ using a 4th-order predictor-corrector method.^{14, 15)} For other lattice sizes and temperatures, we used a new algorithm^{18, 19)} based on 4th-order Suzuki-Trotter decompositions of exponential operators, with a time step $\Delta t = 0.2J^{-1}$. The larger integration time step allowed us to extend the maximum integration time to much larger values than was previously possible.

In order to reduce the computer resources needed we calculated partial spin sums "on the fly",^{14, 15)} however, data could then only be kept for the $(q, 0, 0)$, $(q, q, 0)$ and (q, q, q) directions with q determined by the periodic boundary conditions,

$$q = \frac{2\pi n}{L}, \quad n = \pm 1, \pm 2, \dots, \pm(L-1), L. \quad (2.5)$$

Since all three Cartesian spatial directions are equivalent by symmetry, results for $(q, 0, 0)$, $(0, q, 0)$ and $(0, 0, q)$ were averaged. Similarly, the same operations carried out for the $(q, q, 0)$ and (q, q, q) directions were also averaged over the equivalent reciprocal lattice directions.

For the Heisenberg ferromagnet the order parameter is the total magnetization, which is a conserved quantity. Thus the dynamic structure factor $S(\mathbf{q}, \omega)$ can be separated into a component along the axis of the total magnetization (longitudinal component) and a transverse component; however, for the isotropic antiferromagnet considered here the order parameter is not conserved and the longitudinal and transverse components of $S(\mathbf{q}, \omega)$ cannot be separated in the simulation. Henceforth we will use the term dynamic structure factor to refer to the average.

Two practical limitations on spin-dynamics techniques are the finite lattice size and the finite evolution time. The finite time cutoff can introduce oscillations in $S(\mathbf{q}, \omega)$, which can be smoothed out by convoluting the spin-spin correlation function with a resolution function in frequency. In neutron scattering experiments the divergence of the neutron beam gives rise to an intrinsic Gaussian resolution function in \mathbf{q} and ω and the smoothed dynamic structure factor is

$$\begin{aligned} \bar{S}_{\xi}^k(\mathbf{q}, \omega) &\equiv \sum_{\mathbf{R}} e^{i\mathbf{q}\cdot\mathbf{R}} \int_{-t_{cutoff}}^{+t_{cutoff}} e^{i\omega t} C^k(\mathbf{R}, t) e^{-\frac{(t\delta_{\omega})^2}{2}} \frac{dt}{2\pi} \\ &\approx \frac{1}{\sqrt{2\pi}\delta_{\omega}} \int_{-\infty}^{+\infty} S_{\xi}^k(\mathbf{q}, \omega') e^{-\frac{(\omega-\omega')^2}{2\delta_{\omega}^2}} d\omega', \end{aligned} \quad (2.6)$$

where δ_{ω} is a parameter characterizing the Gaussian resolution function and has to be chosen properly so that effects due to the finite time cutoff can be neglected. The momentum dependent susceptibility, $\bar{\chi}_{\xi}^k(\mathbf{q})$, is given by

$$\int_{-\infty}^{\infty} \bar{S}_{\xi}^k(\mathbf{q}, \omega) \frac{d\omega}{2\pi} = \bar{\chi}_{\xi}^k(\mathbf{q}). \quad (2.7)$$

Finite-size scaling theory^{14, 20)} can be used to extract the dynamic critical exponent z : the divergence of the correlation length ξ is limited by L and the dynamic finite-size relations are given by

$$\frac{\omega \bar{S}_L^k(\mathbf{q}, \omega)}{\bar{\chi}_L^k(\mathbf{q})} = G(\omega L^z, qL, \delta_{\omega} L^z) \quad (2.8)$$

and

$$\bar{\omega}_m = L^{-z} \bar{\Omega}(qL, \delta_{\omega} L^z), \quad (2.9)$$

where $\bar{\omega}_m$ is a characteristic frequency, defined as

$$\int_{-\bar{\omega}_m}^{\bar{\omega}_m} \bar{S}_L^k(\mathbf{q}, \omega) \frac{d\omega}{2\pi} = \frac{1}{2} \bar{\chi}_L^k(\mathbf{q}). \quad (2.10)$$

For $t_{cutoff} \geq 400J^{-1}$ the oscillations in the dynamic structure factor were not very significant. Thus, we first estimate the dynamic critical exponent z without using a resolution function, i.e. we take $\delta_{\omega} = 0$. In this case z can be obtained from the slope of a graph of $\log(\omega_m)$ vs $\log(L)$ (where ω_m is the characteristic frequency for $\delta_{\omega} = 0$) if qL is fixed and L is large enough to be in the asymptotic-size regime.

The effects of the small oscillations in $S(q, \omega)$ on the dynamic exponent z can be evaluated by repeating the analysis using a resolution function so that the function $\bar{\Omega}(qL, \delta_{\omega} L^z)$ in Eq. (2.9) is constant if qL and $\delta_{\omega} L^z$ are

fixed and

$$\bar{\omega}_m \sim L^{-z}. \quad (2.11)$$

Because δ_ω depends on z , this exponent had to be determined iteratively. An initial value $z^{(0)}$ was used to determine δ_ω for different L , $\bar{S}_L^k(\mathbf{q}, \omega)$ and $\bar{\omega}_m$ were computed for different values of L and q with qL held fixed (i.e. n is constant) and a new estimate, $z^{(1)}$, was extracted from Eq. (2.11). This procedure is repeated until the estimates converge.

§3. Results

3.1 Numerical data for $S(\mathbf{q}, \omega)$

For $T \leq T_c$ our results for the dynamic structure factor show a spin-wave and a central peak. At low temperatures the central peak is barely visible and very narrow spin wave peaks are the dominant feature, see Fig. 1 (finite-size effects are evident for $n = 1$). In Fig. 2 we show lineshapes for lattice size $L = 60$ at $T = 0.9T_c$ and several q -values in the [100] direction. As q increases, the central peak broadens and its relative amplitude increases. As the temperature is increased, the central peak grows, and at T_c the central peak is even stronger than the spin wave peak. Fig. 3 shows lineshapes for $L = 60$ and $q = \pi/15$ and $3\pi/10$ in the [100] direction. Clearly oscillations due to the finite t_{cutoff} are negligible; therefore, in our lineshape analysis we did not use a resolution function. For direct comparison with experimental data we convoluted our results with a Gaussian

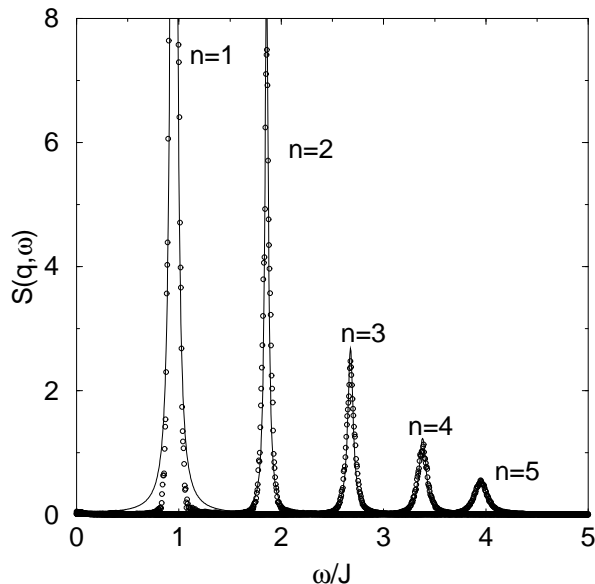


Fig. 1. Dynamic structure factor $S(\mathbf{q}, \omega)$ from our simulations for $L = 20$ at $T = 0.4T_c$, q in the [100] direction. The symbols represent spin dynamics data and the solid line is a fit with the Lorentzian function given in Eq. (3.1).

resolution function with the same width as in the experiment. The structure in the lineshapes discussed here is much larger than our resolution in frequency. Below T_c , previous theoretical¹⁰⁾ and experimental⁹⁾ studies provided the comparison of the position and the half-width

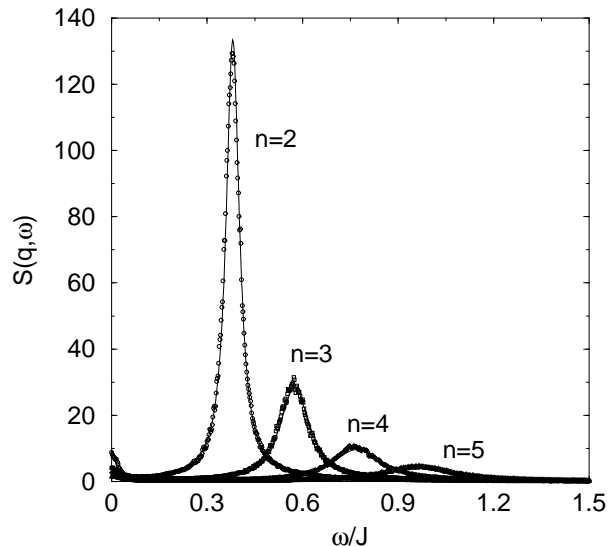


Fig. 2. Dynamic structure factor $S(\mathbf{q}, \omega)$ for $L = 60$ at $T = 0.9T_c$, and q in the [100] direction. The symbols represent spin dynamics data and the solid line is a fit with the Lorentzian function given in Eq. (3.1).

of the spin-wave and central peaks by fitting the lineshape to a Lorentzian form

$$S(\mathbf{q}, \omega) = \frac{A\Gamma_1^2}{\Gamma_1^2 + \omega^2} + \frac{B\Gamma_2^2}{\Gamma_2^2 + (\omega + \omega_s)^2} + \frac{B\Gamma_2^2}{\Gamma_2^2 + (\omega - \omega_s)^2} \quad (3.1)$$

where the first term corresponds to the central peak and the last two terms are from the spin-wave creation and annihilation peaks at $\omega = \pm\omega_s$.

For $T = 0.9T_c$ Lorentzian lineshapes fit our results well for small values of q , except for the smallest value, $q = 2\pi/L$, in the [100] direction for which finite size effects are apparent. For large values of q the Lorentzian form given in Eq. (3.1) does not fit the data, especially at high frequency. In general, the fitted parameters varied when different frequency ranges were used in the fit by an amount which was often larger than the statistical error in the fitted parameters obtained from the fit using a single frequency range. Therefore, for $T = 0.9T_c$ we estimated the error in the fitted parameters by fitting the lineshapes using three different ranges of frequency and taking the average. At T_c , renormalization-group theory (RNG)¹¹⁾ predicts a non-Lorentzian functional form for the spin-wave lineshape, which has been used along with a Lorentzian central peak to analyze experimental data.⁹⁾ Since it is more complicated to perform fits to this RNG functional form and since the spin-wave peaks obtained from the simulations are more pronounced than in the experiment, and thus less dependent on the fitted functional, we have fitted the lineshapes at T_c to Lorentzians, as given in Eq. (3.1). Although obtaining a good fit to our data at T_c was more difficult than below T_c , the resulting fits are still reasonable. Unlike for $T = 0.9T_c$, at T_c the lineshape parameters used in the analysis below are the values obtained from the fit to only one frequency range, which was the one that gave the best fit. The actual error in the fitted parameters at T_c should be larger (by up to a factor of 5) than the error

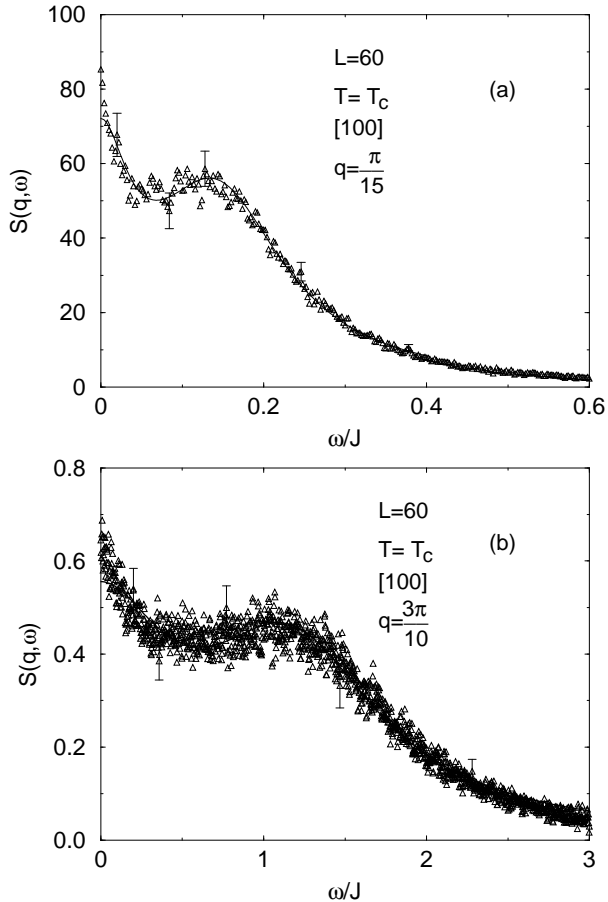


Fig. 3. Dynamic structure factor $S(\mathbf{q}, \omega)$ at $T = T_c$: (a) $q = \pi/15$ and (b) $3\pi/10$ in the [100] direction. The symbols represent spin dynamics data for $L = 60$ and the solid line is a fit to the sum of Lorentzians given in Eq. (3.1). Error bars are only shown for a few typical points; at high frequency they are of the size of the fluctuations in the data.

bars shown in the figures below. Illustrations of the fits using Eq. (3.1) to the simulated lineshapes at $T = 0.9T_c$ and at T_c for several values of q are shown in Figs. 2 and 3.

We also found very weak peaks in the high frequency tail of the spin-wave peaks. Using the spin-wave frequencies in the [100], [110] and [111] directions we could check that the position of these extra peaks corresponded to frequencies of two spin-wave addition peaks. These extra structures in the lineshapes were particularly visible for the smallest q -values.

Fig. 4 shows how the dispersion curve varies as the temperature increases from $T = 0$ to T_c . Although the Lorentzian in Eq. (3.1) did not yield good fits to the lineshapes for larger values of q , the spin-wave peak positions could still be determined relatively accurately and the dispersion curve could be measured up to $q = \pi/2$. Well below T_c , the dispersion relation is linear for small q , but as the temperature increases towards T_c , the dispersion relation changes gradually to power-law

$$\omega_s = A_s q^x. \quad (3.2)$$

For $T = 0.9T_c$ and $L = 60$ a fit to the smallest five

q values of the dispersion curve to Eq. (3.2) yielded $x = 1.017 \pm 0.003$. If larger values of q are included in the fit, the exponent decreased slightly. The sensitivity of the fitted exponent to the particular form of the fitted function was examined by including a quadratic term, i.e.,

$$\omega_s = A_s q^x + B_s q^2, \quad (3.3)$$

yielding a similar value $x = 1.020 \pm 0.003$. When larger values of q were included in the fits, Eq. (3.3) tended to yield smaller χ^2 's per degree of freedom than Eq. (3.2). The dispersion curve for $T = T_c$ and $L = 60$ fitted to Eq. (3.2) yielded an exponent of $x = 1.38 \pm 0.01$ when the smallest 12 values of q were included in the fit. As the larger q were excluded from the fit, the exponent increased slightly, tending towards $x \simeq 1.40$. When only the smallest few values of q were included in the fit, the exponent decreased again, reflecting the fact that we probed correlations between spins separated by larger distances, i.e. smaller q . This reflected the finite size of the lattice (and thus of the correlation length), showing that the system is not at criticality. Hence, the exponent x decreases towards unity. In contrast, large values of q correspond to short distance (in the direct lattice space) spin-spin correlations, and the correlation length is much larger than the distance probed. Our results at T_c agree with recent experiment⁹⁾ which found $x = 1.43 \pm 0.04$ when the dispersion curve at T_c was fitted to a power-law relation of the form given in Eq. (3.2). The solid lines in Fig. 4 are fits to Eq. (3.3); in general, these fits gave lower values of χ^2 per degree of freedom than fits to Eq. (3.2). In the critical region, dynamic scaling theory predicts²¹⁾ that the half-width of spin-wave peaks behaves as $\Gamma_2 \sim q^{1.5}$, whereas for the hydrodynamic regime the prediction from hydrodynamic theory²²⁾ is $\Gamma_2 \sim q^2$. The half-width of the spin-

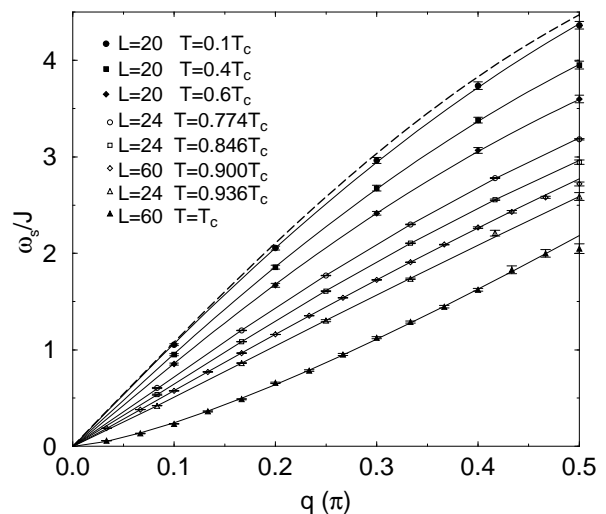


Fig. 4. Spin-wave dispersion relations for $T \leq T_c$, in the [100] direction. The symbols represent spin-wave positions extracted from Lorentzian fits to the lineshapes from the simulations, and the solid curves are fits of the dispersion relations at different temperatures to Eq. (3.3).

wave peaks at $T = 0.9T_c$ and $L = 60$ from our simula-

tions is shown in Fig. 5. We observed a crossover from $\Gamma_2 = (0.401 \pm 0.004)q^{1.46 \pm 0.06}$ for larger values of q to the behavior $\Gamma_2 = (0.48 \pm 0.02)q^{1.86 \pm 0.05}$ for small values of q . The behavior for relatively large q agrees with dynamic scaling theory and with recent experiment.⁹⁾ The exponent we obtained by fitting only small values of q is close to the hydrodynamic prediction. Thus, the spin-

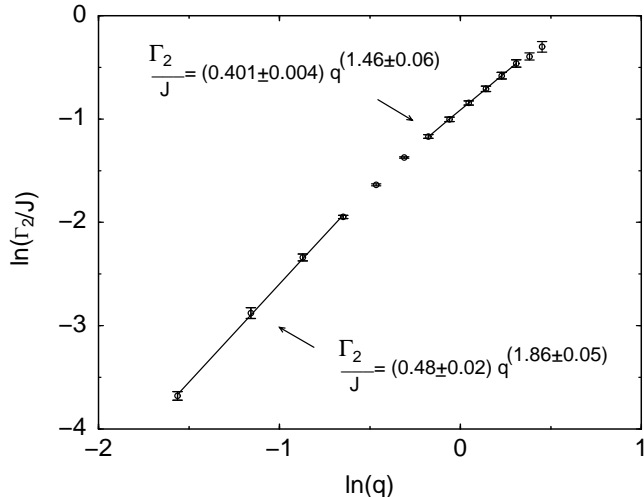


Fig. 5. Log-log graph of the half-width of the spin-wave peak extracted from Lorentzian fits to the lineshapes obtained from simulations for $L = 60$ and $T = 0.9T_c$ in the $[100]$ direction as a function of q .

wave half-width reflected crossover between two different regimes, the critical and the hydrodynamic regions. This crossover is similar to the one observed in the dispersion curve at T_c , discussed above. For $T = T_c$ and $L = 60$ the spin-wave half-width also had a power-law behavior which varied from approximately $q^{1.2}$ when the 12 smallest values of q were included to $\sim q^{1.4}$ when only the smallest five wave-vectors were considered. In their recent experiment, Coldea *et al.*⁹⁾ found $\Gamma_2 = Dq^{1.41 \pm 0.05}$ for $0.77T_c \leq T < T_c$, and the coefficient D increased with increasing temperature.

As in the experiments, the dynamic structure factors from our simulations had central peaks ($\omega = 0$) for $T \leq T_c$. In contrast, RNG theory predicts a central peak in the longitudinal component of the dynamic structure factor only below T_c ,¹⁰⁾ and none of the theories predict a central peak at T_c .^{11,12)} For $T = 0.9T_c$ and $L = 60$ fits of the central peak half-width to a simple power law were poor, but a much improved fit was obtained by using the function $\Gamma_1 = A_1 + B_1q^{C_1}$, which allows for a non-zero central peak width when q vanishes. In these fits the data for the smallest possible q , i.e. $n = qL/2\pi = 1$, were excluded because of large finite-size effects. The fit including data for q corresponding to $n = 2$ until $n = 7$ yielded $A_1 \simeq 0.013 \pm 0.001$, $B_1 \simeq 0.120 \pm 0.005$ and $C_1 \simeq 2.4 \pm 0.2$. As we systematically included larger values of q in the fits, these parameters decreased slightly. At T_c we also fitted the central peaks to Lorentzians, according to Eq. (3.1); however, these tended to yield curves with smaller amplitudes than the data. Since there is no theoretic-

cal prediction for the central peak, we have also tried to fit them with a Gaussian form but the result was much worse than with Lorentzians.

The lattice sizes that we used were all multiples of 12 so there were certain q -values which were common to all L . Lineshapes and spin-wave peak positions could be compared for different L at a fixed value of q . At $T = 0.9T_c$ we saw no significant finite-size effect for $L \geq 24$; however, when we superimposed lineshapes at T_c for fixed q , and different values of L , finite-size effects were noticeable for $L = 24$. For larger L the lineshapes were the same within the error bars.

The dynamic critical exponent z was extracted from finite-size scaling of $\bar{\omega}_m$. From an analysis without resolution function, or equivalently $\delta\omega = 0$, and $n = 1, 2$, we estimated $L = 30$ to be approximately the onset of the asymptotic-size regime and $z = 1.45 \pm 0.01$ for $n = 1$ and $z = 1.42 \pm 0.01$ for $n = 2$. We also estimated the value of z using a resolution function. Several initial values of $z^{(0)}$ were used, and in all cases the exponent z converged rapidly. Our final estimate for the dynamic critical exponent is $z = 1.43 \pm 0.03$. Analyses of the characteristic frequency $\bar{\omega}_m$ as a function of L with and without a resolution function agreed closely.

3.2 Comparison with experiment for $RbMnF_3$

We now compare our results with the recent neutron scattering data of Coldea *et al.*⁹⁾ The Mn^{2+} ions in $RbMnF_3$ have spin $S = 5/2$ and interact via a quantum Heisenberg Hamiltonian of the form

$$\mathcal{H} = J^{exp} \sum_{\langle \mathbf{r}\mathbf{r}' \rangle} \mathbf{S}_{\mathbf{r}}^Q \cdot \mathbf{S}_{\mathbf{r}'}^Q, \quad (3.4)$$

where $\mathbf{S}_{\mathbf{r}}^Q$ are spin operators with magnitude $|\mathbf{S}_{\mathbf{r}}^Q|^2 = S(S+1)$ and the interaction strength between pairs of nearest-neighbors was determined experimentally⁴⁾ to be $J^{exp} = (0.58 \pm 0.06)$ meV. In contrast, our simulations were performed on a classical Hamiltonian; however, quantum Heisenberg systems with large spin values ($S \geq 2$) have been shown to behave as classical Heisenberg systems where the spins are vectors of magnitude $\sqrt{S(S+1)}$ with the same interaction strength between pairs of nearest neighbors as in the quantum system.²³⁾ Since our classical spins were vectors of unit length, a normalization of the interaction strength J from our simulation is needed, i.e.

$$J = J^{exp} S(S+1). \quad (3.5)$$

Although this choice leaves the Hamiltonian unchanged, it modifies the equations of motions given above as Eq. (2.2). The dynamics of the classical system so defined is the same as the quantum system defined by the Hamiltonian in Eq. (3.4) if one rescales the time, or equivalently, the frequency. We obtain

$$\omega^{exp} = J^{exp} \sqrt{S(S+1)} \frac{w}{J}, \quad (3.6)$$

where ω^{exp} is the frequency transfer in the quantum system, measured experimentally, and w/J is the frequency transfer in units of J from our simulations. Note that the critical temperature of the classical Heisenberg

model has been determined from Monte Carlo simulations¹⁷⁾ to be $T_c = 1.442929(77)J$. Using the normalization for the interaction strength J given in Eq. (3.5) and the experimental value $J^{exp} = (6.8 \pm 0.6)\text{K}^4$ we get $T_c = (85.9 \pm 7.6)\text{K}$ which is well within the error bars of the experimental value of around 83K.

Neutron scattering experiments measure the dynamic structure factor multiplied by a temperature and frequency dependent population factor,^{9,24,25)} and this factor was removed from the experimental data before comparing them with the simulational data. Another complication in the experiment is the finite divergence of the neutron beam which gives rise to a resolution function which is usually approximated by a Gaussian in the 4-dimensional energy and wave-vector space. In the experiment,⁹⁾ the measured resolution width along the energy axis was 0.25 meV (full-width at half-maximum) for incoherent elastic scattering. In order to directly compare our results with the experiment, we convoluted the lineshapes from our simulation with a Gaussian resolution function in energy with the experimental value of full-width at half-maximum, normalized according to Eq. (3.6). The standard deviation δ_ω thus obtained for the Gaussian resolution function in Eq. (2.6) was 0.0619 in units of J . (Convolution of our lineshapes with the experimental 3-dimensional Gaussian function in the wave-vector space had a negligible effect.)

The experimental data⁹⁾ are from constant- q scans with both positive and negative energy transfer. The wave-vector transfer \mathbf{Q} was measured along the [1,1,1] direction, around the antiferromagnetic zone center which in our notation is the (π, π, π) point. Note that Coldea *et al*⁹⁾ define the wave-vector transfer \mathbf{Q} in units such that the antiferromagnetic zone center is $(0.5, 0.5, 0.5)$; hence, to express their \mathbf{Q} in units of \AA^{-1} one has to multiply it by $2\pi/a$, where a is the cubic lattice parameter expressed in \AA . However, in the simulation direct lattice positions are defined in units of the lattice constant a ; thus we obtain wave-vectors multiplied by the constant a . We emphasize that one has to divide the wave-vector \mathbf{Q} [and also q , see Eq. (2.5)] defined in this paper by 2π in order to express it in the units used by Coldea *et al*.⁹⁾ In the experiment, measurements were taken for wave-vectors $\mathbf{Q} = (\pi + q, \pi + q, \pi + q)$, with $q = 2\pi(0.02), 2\pi(0.04), \dots, 2\pi(0.12)$, but unfortunately these values of q are not accessible in our simulations for the particular lattice sizes that we used. Thus, direct comparison of the lineshapes from the simulation with the experimental ones required interpolation of our results to obtain the same q values as the experiment. This was done by first fitting our lineshapes with a Lorentzian form, as given in Eq. (3.1). Since the parameters B , Γ_2 and ω_s obtained from these fits behave as power-laws of q , we linearly interpolated the logarithm of these parameters as a function of the logarithm of q , to obtain new parameters for the lineshapes corresponding to those values of q actually observed in the experiment. We estimated the uncertainties from this procedure to be less than five percent for the parameter B , less than three percent for the spin-wave half-width Γ_2 and the spin-wave position ω_s at T_c , and less than one percent for the spin-wave position

ω_s at $T = 0.9T_c$. Below T_c , the parameters A and Γ_1 associated with the central peak were linearly interpolated, yielding new values with uncertainties of approximately five percent. At T_c , the parameter A was interpolated in the log-log plane (as for B , Γ_2 and ω_s discussed above), whereas Γ_1 was simply linearly interpolated. The uncertainties in A and Γ_1 at T_c were estimated to be less than ten percent. For $L = 60$, there is one value of q , namely $q = 2\pi(0.10)$, which is accessible to both simulation and experiment. This was the only case for which we did not have to interpolate in q .

Our results at the critical temperature can be compared with the experimental data at the same temperature. Below T_c , the simulations are mainly for $T = 0.9T_c$ which unfortunately does not coincide with any temperature used in the experiment; however, it is very close to $T = 0.894T_c$ for which experimental results are available. To correct for the slight difference, we made a linear interpolation in temperature, using our results for $L = 24$ at $T = 0.846T_c$ and at $T = 0.9T_c$. We first fitted the lineshapes at these two temperatures to the form given by Eq. (3.1), then we linearly interpolated the position and the amplitude of the spin-wave peak at these temperatures, to obtain the spin-wave position and amplitude corresponding to $T = 0.894T_c$. For small values of q we found that the frequency and amplitude of the spin-wave peak at $T = 0.894T_c$ were respectively ~ 1.5 and 5 percent larger than at $T = 0.9T_c$ and this difference decreased for larger values of q .

The intensity of the lineshapes in the neutron scattering experiment was measured in counts per 15 seconds. For both temperatures $T = 0.894T_c$ and $T = T_c$ the measurements for the several wave-vectors were done with the same experimental set-up and conditions. Therefore, the relative intensities of the lineshapes for the different wave-vectors is fixed, and equal for both temperatures. The intensity of the lineshapes obtained in the simulation had to be normalized to the experimental value; however, because the relative intensities for different wave-vectors is fixed, we have only one independent normalization factor for all the wave-vectors at both temperatures. The normalization of the intensity was chosen so that the spin-wave peak for $T = 0.894T_c$ and $q = 2\pi(0.08)$ from the experiment and the simulation matched. This same factor was used to normalize the intensities of the lineshapes corresponding to the remaining values of wave-vectors at $T = 0.894T_c$, and for all cases at T_c .

The final lineshapes for $T = 0.894T_c$, $L = 60$, and two wave-vectors are shown in Fig. 6 together with experimental lineshapes for each case. Fig. 7 shows the comparison of the dispersion curve from the simulation and the experiment at $T = 0.894T_c$. Good agreement between our results and experiment can be seen from either the direct comparison of the lineshapes, or the comparison of the dispersion curve. The lineshape intensities from simulation and experiment agree over two orders of magnitude, from $q = 2\pi(0.02)$ to $q = 2\pi(0.10)$. Fig. 8 shows the comparison of lineshapes from the simulation and the experiment for $T = T_c$, $L = 60$, and two values of q . The dispersion curve obtained from the simulations at $T = T_c$, shown in Fig. 7, is systematically larger than

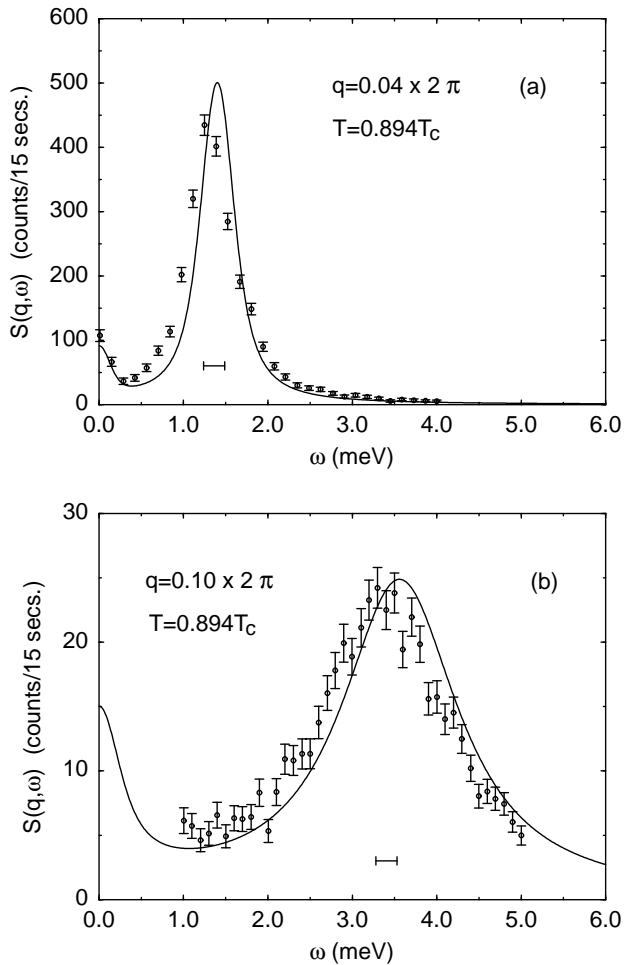


Fig. 6. Comparison of lineshapes obtained from fits to simulation data for $L = 60$ (solid line) and experiment (dots) at $T = 0.894T_c$ in the [111] direction. The horizontal line segment in each graph shows the resolution in energy (full-width at half-maximum).

the experimental values. We emphasize that the error bars shown for the dispersion curve obtained from our simulations at T_c reflect only the statistical errors of a best fit of the lineshapes. For each q , this fit was done with only one range of frequency; hence errors associated with the choice of frequency range and the quality of the fit were not taken into account. It is reasonable to expect that such sources of error would increase the error bars by a factor of 5. From the direct comparison of the simulated and experimental lineshapes at T_c it is difficult to determine the difference in the spin-wave frequencies, because the spin-wave peaks from the experiment are not very pronounced, and their positions have to be extracted from the fits of the lineshapes. As mentioned earlier, the experimental data at T_c were fitted to a functional form predicted by RNG theory plus a Lorentzian central peak. The quality of the fitting can be seen in Fig. 8(b) for $q = 2\pi(0.08)$, along with the RNG component of the fit and the prediction by mode-coupling theory. Finally, even though at T_c the lineshape intensities from the simulations for small frequency transfer tended to be lower as compared to the experiment, the agreement is still reasonably good, con-

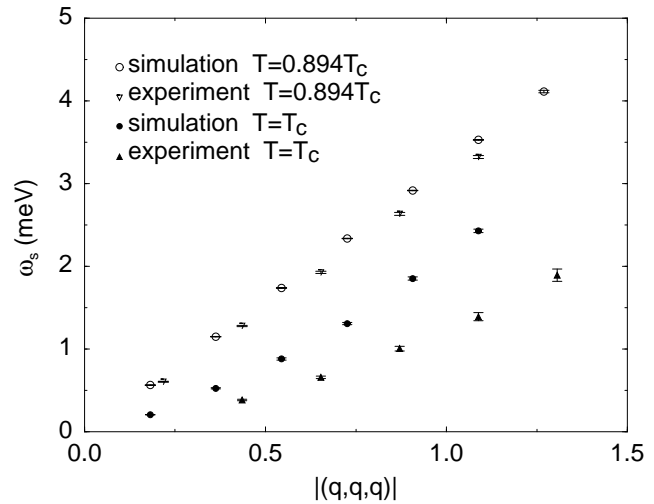


Fig. 7. Comparison of the dispersion curve at $T = T_c$ and $T = 0.894T_c$ obtained from simulations for $L = 60$ (circle) and the experiment (triangle), in the [111] direction. The simulation data shown here correspond to values of q accessible with $L = 60$, without interpolation to match the q values from the experiment. In this notation, the first Brillouin zone edge is at $|(q, q, q)| \simeq 2.72$.

sidering the variation of the intensities over almost two orders of magnitude from $q = 2\pi(0.02)$ to $q = 2\pi(0.12)$.

§4. Conclusion

We have studied the magnetic excitations and the dynamic critical properties of the classical Heisenberg antiferromagnet on a simple cubic lattice using large-scale spin dynamics simulations. A new 4th-order decomposition integration technique as implemented in Ref.19 allowed us to use a larger time integration step thus extend the maximum integration time to much larger values than was previously possible.

Below T_c , the dispersion curves were approximately linear for small q . Increasing the temperature towards the critical temperature the dispersion curve became a power-law, reflecting the crossover from hydrodynamic to critical behavior. The spin-wave half-width at $T = 0.9T_c$ also showed a crossover from critical behavior at large values of q to hydrodynamic behavior at small values of q . The dynamic critical exponent was estimated to be $z = (1.43 \pm 0.03)$ which is in agreement with the experimental value of Coldea *et al*⁹⁾ and slightly lower than the dynamic scaling prediction.

We made direct, quantitative comparison of both the dispersion curve and the lineshapes obtained from our simulations with the recent experimental results by Coldea *et al*⁹⁾ for RbMnF_3 . At $T = 0.894T_c$ the agreement was quite good with the major difference being at T_c where spin-wave peaks from our simulations tended to be at slightly larger frequencies than the experimental results. Both at $T = 0.894T_c$ and at T_c the lineshape intensities varied over almost two orders of magnitude from $q = 2\pi(0.02)$ to $q = 2\pi(0.10)$ and there was good agreement between the intensities from simulation and experiment over the entire range. Thus, the simple

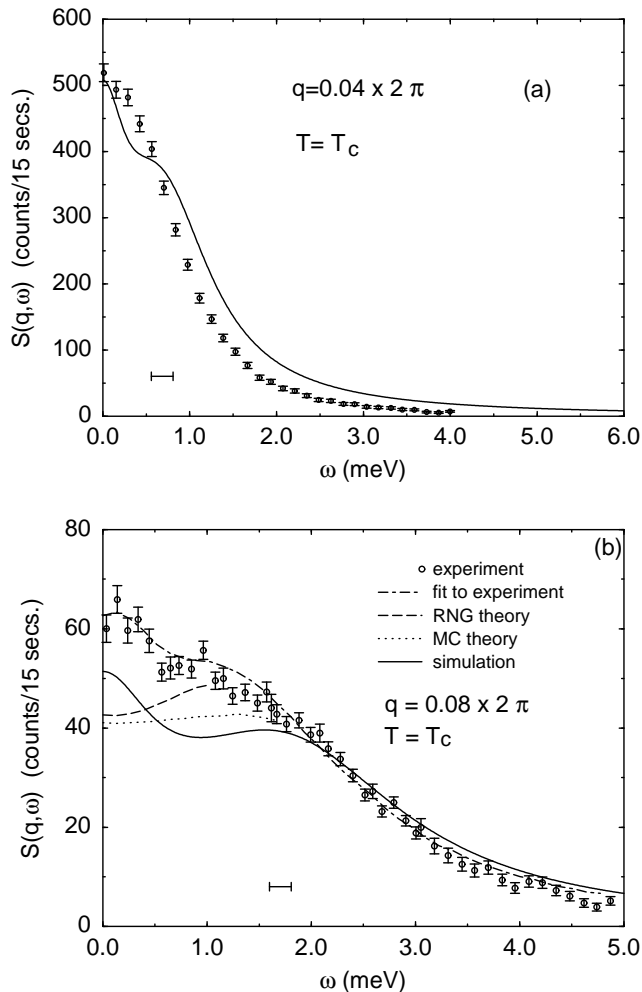


Fig. 8. Comparisons of lineshapes obtained from fits to simulation data for $L = 60$ (solid line) and the experiment (open circles) at $T = T_c$ in the $[111]$ direction, for (a) $q = 2\pi(0.04)$ and (b) $q = 2\pi(0.08)$. The dot-dashed line in (b) is a fit of the experimental data to the functional form predicted by the RNG theory plus a Lorentzian central peak, and the RNG component of the fit is shown by the long-dashed line. The prediction of Mode Coupling (MC) theory is shown by the dotted line in (b). The horizontal line segment in each graph represents the resolution in energy (full-width at half-maximum).

isotropic nearest-neighbor classical Heisenberg model describes the dynamic behavior of this real magnetic system quite well.

ACKNOWLEDGMENTS

We thank R. A. Cowley and R. Coldea for helpful discussions and for sending us their data. We also thank M. Krech and H. B. Schüttler for valuable discussions. Simulations were carried out on the Cray T90 at the San Diego Supercomputing Center, and on a SGI Origin2000 and IBM R6000 machines in the University of Georgia. This research was supported in part by NSF Grant No. DMR-9727714.

- [3] A. Kornblit and G. Ahlers, Phys. Rev. B **8**, 5163 (1973).
- [4] C. G. Windsor and R. W. H. Stevenson, Proc. Phys. Soc. (London) **87**, 501 (1966); C. G. Windsor, D. H. Saunderson, and E. Schedler, Phys. Rev. Lett. **37**, 855 (1976).
- [5] D. T. Teaney, M. J. Freiser, and R. W. H. Stevenson, Phys. Rev. Lett. **9**, 212 (1962).
- [6] M. J. Freiser, P. E. Seiden, and D. T. Teaney, Phys. Rev. Lett. **10**, 293 (1963).
- [7] A. Tucciarone, H. Y. Lau, L. M. Corliss, A. Delapalme, and J. M. Hastings, Phys. Rev. B **4**, 3206 (1971).
- [8] U. J. Cox, R. A. Cowley, S. Bates, and L. D. Cussen, J. Phys.: Condens. Matter **1**, 3031 (1989).
- [9] R. Coldea, R. A. Cowley, T. G. Perring, D. F. McMorrow, and B. Roessli, Phys. Rev. B **57**, 5281 (1998).
- [10] G. F. Mazenko, M. J. Nolan, and R. Freedman, Phys. Rev. B **18**, 2281 (1978).
- [11] R. Freedman and G. F. Mazenko, Phys. Rev. Lett. **34**, 1575 (1975); Phys. Rev. B **13**, 4967 (1976).
- [12] A. Cuccoli, S. W. Lovesey, and V. Tognetti, J. Phys.: Condens. Matter **6**, 7553 (1994).
- [13] P. C. Hohenberg and B. I. Halperin, Rev. Mod. Phys. **49**, 435 (1977).
- [14] K. Chen and D. P. Landau, Phys. Rev. B **49**, 3266 (1994).
- [15] A. Bunker, K. Chen, and D. P. Landau, Phys. Rev. B **54**, 9259 (1996).
- [16] R. W. Gerling and D. P. Landau, Phys. Rev. B **41**, 7139 (1990).
- [17] K. Chen, A. M. Ferrenberg, and D. P. Landau, Phys. Rev. B **48**, 3249 (1993).
- [18] J. Frank, W. Huang, and B. Leimkuhler, J. Comp. Phys. **133**, 160 (1997).
- [19] M. Krech, A. Bunker and D. P. Landau, Comp. Phys. Comm. **111**, 1 (1998).
- [20] D. C. Rapaport and D. P. Landau, Phys. Rev. E **53**, 4696 (1996).
- [21] B. I. Halperin and P. C. Hohenberg, Phys. Rev. Lett. **19**, 700 (1967); Phys. Rev. **177**, 952 (1969).
- [22] B. I. Halperin and P. C. Hohenberg, Phys. Rev. **188**, 898 (1969).
- [23] See for example, M. E. Fisher, Rep. Prog. in Phys. **30**, 615 (1967); F. Keffer, in *Handbuch der Physik*, vol. 18/2, edited by H. P. J. Wijn (Springer-Verlag, Heidelberg, 1966).
- [24] M. F. Collins, *Magnetic Critical Scattering* (Oxford University Press, New York, 1989).
- [25] S. W. Lovesey, *Theory of Neutron Scattering from Condensed Matter* (Clarendon, Oxford, 1984).

[1] S. J. Pickart, H. A. Alperin, and R. Nathans, J. Phys. **25**, 565 (1964).

[2] D. T. Teaney, V. L. Moruzzi, and B. E. Argyle, J. Appl. Phys.